https://doi.org/10.5194/acp-2019-273
Preprint. Discussion started: 8 July 2019

Atmospheric Chemistry and Physics Discussions

The effect of low density over the "roof of the world" Tibetan Plateau on the triggering of convection

Yinjun Wang[1], Xiangde Xu[1], Mingyu Zhou[2], Donald H. Lenschow[3], Xueliang Guo[1], Yang Zhao[1], and Bin Chen[1]

[1] State Key Laboratory of Severe Weather, Chinese Academy of Meteorological Sciences, Beijing, China,

[2] National Marine Environmental Forecasting Center, Beijing, China,

[3] National Center for Atmospheric Research, Boulder CO, USA

Correspondence to: Xiangde Xu (xuxd@cma.gov.cn)

Abstract

We study the relationships between convective characteristics and air density over the Tibetan Plateau (TP) from the perspective of both climate statistics and large eddy simulation (LES). First, based on climate data, we found that there is stronger thermal turbulence and higher frequency of low cloud formation for the same surface relative humidity over the eastern and central TP compared with the eastern monsoon region of China. Second, we focus on the dynamical and thermal structure of the atmospheric boundary layer (ABL) with low air density. With the same surface heat flux, a decrease in air density enhances the buoyancy flux, which increases the ABL depth and moisture transport from the subcloud layer into the cloud layer. With the same low cloud cover for different air densities, the greater ABL depth for lower air density means that the average mixed-layer relative humidity with higher air density will be greater than that with low air density. Results from a subcloud convective velocity scaling scheme were compared with LES results, which indicated that the original fixed parameter values in this scheme may not adequate in case of lower relative humidity and weaker thermal turbulence in the subcloud layer.

Key words: Tibetan Plateau, air density, convective boundary layer, shallow cumulus, large eddy simulation

1 Introduction

The Tibetan Plateau (TP), which resembles a "third pole" and a "world water tower", plays an important and special role in the global climate and energy–water cycle (Xu et al., 2008). Cumulus convection over the TP transfers heat, moisture and momentum to the free troposphere, which can impact the atmospheric circulation regionally and globally (Li and Zhang 2016). (Dai,1990) conducts statistics of the

https://doi.org/10.5194/acp-2019-273
Preprint. Discussion started: 8 July 2019

Atmospheric Chemistry and Physics Discussions

proportion of different cloud types in different regions, the results show that cumulonimbus clouds over the center of the TP account for 21%, which is about five times than that of over the rest of China. The elevated land surface with strong radiative heating makes the massive TP a favorable region for initiating numerous convective cells, and has a high frequency of cumulonimbus or mesoscale convective systems (MCSs) (Sugimoto and Ueno, 2012). Li and Zhang (2016) confirmed that the climatological occurrence of cumulus over the TP is significantly greater than over the surrounding area by using four years of CloudSat–CALIPSO satellite data. They found that the ubiquitous cumulus over the northern TP is related to the higher air temperature and larger relative humidity above the surface than those in the surrounding regions at the same height above sea level.

Xu et al. (2002) and Zhou et al. (2000) found that the turbulence with motion at vertical speeds of up to 1 m s^{-1} at a height of about 120 m above the surface with the horizontal scale about 600 m, strong convective plumes and a larger than 2000 m mixed layer may result in ubiquitous "pop-corn-like" convective clouds over the TP. These clouds, which have relatively large vertical and small horizontal scale occurred when the strong vertical motions penetrate the capping inversion layer. They can sometimes evolve into mature super convective cloud clusters. Xu et al. (2002) documented the structure of the distinctive "popcorn-like" cloud systems over the TP by comprehensively analyzing TIPEX II observational data. Xu et al. (2012) conjectured that these clouds may be favored by low air density ρ and strong turbulence. The reduced ρ and enhanced buoyancy production results in turbulent characteristics of the convective boundary layer (CBL) over the plateau that are considerably different from that over the plain (Xu et al., 2012).

The sodar data from TIPEX II and the boundary layer tower data from TIPEX III indicated that the contributions of buoyancy and shear to the turbulence kinetic energy in the lower troposphere were larger over the TP than over the southeastern margin of the TP and the low-altitude Chengdu Plain (Zhou et al., 2000; Wang et al., 2016). Observations also indicated that organized turbulence on the meso- and micro-scale was large due to the abnormally strong solar radiation over the TP (Zhou et al., 2000). Therefore, the question arises as to whether there is a relationship among the formation and evolution of frequent "pop-corn-like" convective clouds, low ρ, and turbulence generation over the TP.

We discuss the above key scientific issues from two aspects: climate statistics and large eddy simulation (LES). Climate statistics are used to study the spatial distributions of summertime low cloud cover (*LCC*). Here low cloud includes the total

https://doi.org/10.5194/acp-2019-273
Preprint. Discussion started: 8 July 2019

Atmospheric Chemistry and Physics Discussions

area of observed cloud cover with cloud base less than 2.5 km above the ground level. In the early stages of development we classify the "pop-corn-like" convective cloud as shallow convective cumulus due to their very small horizontal scale (from tens of meters to a few kilometers). We also use high-resolution LES to simulate the three-dimensional turbulent flow and shallow cumulus. We conducted sensitivity tests to study the effect of varying ρ on the formation and evolution of shallow cumulus, and the interrelation between turbulence and convective motion. The LES is also used to test subcloud convective velocity scaling schemes with varying ρ. Finally, we attempt to explain some of the physical processes determining the climate statistics of summertime low cloud cover over China.

2 Data

The data used here are taken from the following observation and reanalysis products:

2.1 observational data at Nagqu in TIPEX III

a) Turbulent fluxes (sensible and latent heat flux) in the surface layer calculated by the eddy covariance technique. Here we applied EDDYPRO software for eddy covariance data quality control. EDDYPRO is an open source software application developed, maintained and supported by LI-COR Biosciences (Available at www.licor.com/EddyPro).

b) L-band sounding data from the China Meteorological Administration (CMA) operational station, three times a day at 06:00, 12:00 and 18:00 LST.

c) Daily mean climate data from 2479 automatic weather stations (AWS) from 1979 to 2016 in China.

2.2 ERA-Interim reanalysis data

We used the synoptic monthly means derived from the ERA-interim reanalysis surface-layer data every 3 hours for summer from 1979 to 2016. We also used 9 day ERA-interim reanalysis data at standard isobaric levels every 6 hours in summer 2015 to calculate large-scale forcing for the LES. Both of these data sets have a spatial resolution of 0.75 ° x 0.75 °, and all the final results of large-scale forcing are derived from the mean values of grids within a radius of 300 km.

3 The climatic characteristics of summertime low cloud and their correlation with air density

Figure 1(a) presents the following two consistent patterns: 1. Because the atmosphere is easily moistened to saturation with ambient high relative humidity, the *LCC* generally increases with increasing relative humidity at 2 m (RH_{2m}) with constant air

https://doi.org/10.5194/acp-2019-273
Preprint. Discussion started: 8 July 2019

density at 2 m (ρ_{2m}), which is consistent with our common sense. 2. The *LCC* increases approximately parabolically with decreasing ρ_{2m} for RH_{2m} both greater than and less than 75% (corresponding to A region and B region, respectively). That is, more low cloud exists in the high altitude area of the TP with low ρ_{2m} and low RH_{2m} (50% < RH_{2m} < 70%). As shown in Figure 1(b), *LCC* greater than 50% is mainly over mid-eastern TP, and southwestern China. Despite the abundant water vapor over the eastern China monsoon region (ECMR), *LCC* is significantly lower over the ECMR relative to that over the mid-eastern TP. Figure 1(c) shows that there is a large area of *LCC* greater than 35% north of 30 °N in mid-eastern TP with low RH_{2m} (RH_{2m} < 70%) and large surface virtual potential temperature flux $\overline{(w'\theta_v')}_s$ > 0.1 °K m s^{-1} in contrast to the low altitude area.

4 The effect of low air density over the TP on the formation and development of cumuli

Zhu et al. (2002) indicated that shallow cumuli result from the daytime development of the CBL in which buoyancy is the dominant mechanism driving turbulent mixing. Mixing by convective elements, or thermals, is limited by the height of the mixed layer *h*, which is capped by an overlying inversion layer. Whether or not shallow cumuli can form is determined by the thermodynamic properties of the CBL and maximum height of the convective turbulence. In Appendix A we present a simple dry CBL model that illustrates the sensitivity of *h* to air density at the surface. We explore this sensitivity in more detail for the TP region by using LES to analyze the effect of ρ on the formation and evolution of cumuli. The LES model description and simulation setup, and a comparison between the observations and the LES are shown in Appendix B. We analyze in detail the results of control experiment CON, six sensitivity experiments with air densities (1.2ρ_{CON}, 1.4ρ_{CON} , 1.7ρ_{CON}) and relative humidities (1.4$\rho_{CON}RH$0.05, 1.4$\rho_{CON}RH$0.15, 1.4$\rho_{CON}RH$0.3).

4.1 The height of the mixed layer *h* and its growth rate *dh/dt* for varying air density

Zhu et al (2002) showed that with constant water vapor mixture ratio q_T and adiabatic temperature lapse rate $\partial T/\partial z = -\gamma_d$ within the CBL, the relationship between the relative humidity at the top of the surface layer RH_0 and the relative humidity at the top of the mixed layer (ML) RH_h can be written as

$$RH_h \approx RH_0\left(1+\frac{L\gamma_d h}{R_v T_0^2}\right) \tag{1}$$

where L is the enthalpy of vaporization, R_v is the gas constant of water vapor, and T_0 is

https://doi.org/10.5194/acp-2019-273
Preprint. Discussion started: 8 July 2019

Atmospheric Chemistry and Physics Discussions

the temperature at the top of the surface layer. Eq. (1) indicates that RH_h increases with increasing h under conditions of fixed T_0 and RH_0. In this study we use the profiles of virtual potential temperature gradient $\partial\theta_v/\partial z$ to define h as the lowest level for which $\partial\theta_v/\partial z > 2$ K km^{-1}.

The equation for the rate of change of h is given by Betts (1973) and Neggers et al. (2006) as

$$\frac{dh}{dt} = w_e + w_s - M \qquad (2)$$

where w_e and w_s are the entrainment and large scale subsidence velocities, respectively and M is the kinematic mass flux of air transported by clouds from the subcloud to cloud layer. M can be modeled as

$$M = a_{cc} w_{cc} \qquad (3)$$

where a_{cc} and w_{cc} are the maximum cloud core fraction and its corresponding vertical velocity at the same height, respectively. Cloud core is the positively buoyant region with respect to the environment. Here we ignore the differences between the height of maximum a_{cc} and h when we use eq. (2) to calculate w_e. M can be ignored since it is more than an order of magnitude smaller than w_e when a_{cc} < 1%(before about 15:00 LST). However, M cannot be ignored in the developmental stage of cumuli due to larger a_{cc} (after about 15:00 LST), which will be discussed in the subsequent section 4.3. w_s is significantly smaller than w_e in this study, and thus the variation of dh/dt mainly depends on w_e. Figure 2(b) shows the time variations of w_e calculated with eq. (2) in four LES experiments (CON, 1.2ρ_{CON}, 1.4ρ_{CON} , 1.7ρ_{CON}). For the zero-order jump assumption, w_e can be modeled as:

$$w_e = -\frac{\overline{\left(w'\theta_v'\right)_h}}{\Delta_{\theta_v}} = \frac{\beta_1 \overline{\left(w'\theta_v'\right)_s}}{\Delta_{\theta_v}} \qquad (4)$$

where $\overline{(w'\theta_v')_h}$ is the entrainment flux at the top of the CBL, $\overline{(w'\theta_v')_s}$ is the surface buoyancy flux, $\Delta_{\theta v}$ is the virtual potential temperature difference across the inversion, and the proportionality factor β_1 is assumed to be a constant, ~0.2 for free convection (e.g. Sullivan et al., 1998). For constant β_1 Zhu et al (2002) derived the following expression for $\Delta_{\theta v}$:

$$\Delta_{\theta_v} = \frac{\gamma_{\theta_v} \beta_1 h}{1 + \alpha\beta_1} \qquad (5)$$

where $\gamma_{\theta v}$ is the mean virtual potential temperature lapse rate above the ML and α is a subsidence-dependent parameter whose likely maximum range is between 1 and 2. For $w_s = 0$, $\alpha = 2$; and for $dh/dt = 0$ (i.e. $w_e + w_s = 0$), $\alpha = 1$. Substituting eq. (5) into

https://doi.org/10.5194/acp-2019-273
Preprint. Discussion started: 8 July 2019

Atmospheric Chemistry and Physics Discussions

(4), we get

$$w_e = \frac{(1+\alpha\beta_1)}{\gamma_{\theta_v} h}\overline{(w'\theta_v')_s} \tag{6}$$

Therefore, w_e is directly proportional to $\overline{(w'\theta_v')_s}$ and inversely proportional to h and $\gamma_{\theta v}$.

For the four LES experiments (CON, 1.2ρ_{CON}, 1.4ρ_{CON} , 1.7ρ_{CON}) with varying ρ, we can confirm that $\overline{(w'\theta_v')_s}$ is inversely proportional to ρ with constant sensible heat flux $H = \rho c_p \overline{(w'\theta_v')_s}$ as shown in Figure 2(c). As shown in Figure 2 (a)-(d), with increasing air density, the increase in h with time is delayed, and there are also obvious delays in the time of the first occurrence of cumulus clouds and cloud core. The increase in h can be divided into 3 stages: 1. h increases slowly with time when h is less than 0.5 km; 2. the growth rate of h obviously increases between about 0.5 km and 1.5 km; 3. the growth rate of h slows down when h exceeds 1.5 km. In the first stage the strong inversion layer at the top of the nighttime stable boundary layer (SBL) gradually erodes due to surface heating. Compared to the high ρ case, the strong inversion layer vanishes faster for the low ρ case due to larger $\overline{(w'\theta_v')_s}$. During the second stage, the increase of $\overline{(w'\theta_v')_s}$ and decrease of $\gamma_{\theta v}$ lead to larger w_e and thus the growth rate of h. This phenomenon is more obvious for low ρ over the TP. In the final stage, h increases relatively slowly over time, but h is significantly larger for small ρ than for large ρ. There are no significant differences in RH_0 and relative humidity above h for the four LES experiments (CON, 1.4$\rho_{CON}RH$0.05, 1.4$\rho_{CON}RH$0.15, 1.4$\rho_{CON}RH$0.3, Figure omitted). Therefore, we conclude that larger RH_h and more favorable conditions for saturation occur for small ρ compared to large ρ.

4.2 Penetrative convection at the top of a growing mixed layer with varying air density

Penetrative convection at the top of the ML can result in cumulus formation (e.g. Stull, 1988). A forced cloud will form when a thermal reaches the lifting condensation level (LCL), but the top of the forced cloud does not reach its level of free convection (LFC). Condensation and latent heat release are insufficient to produce positive buoyancy within the forced clouds, so they remain shallow and undeveloped. Active clouds have positive buoyancy when the updraft reaches the LFC.

Decreasing ρ leads to an earlier appearance of cloud cores. With increasing ρ, h corresponding to the appearance of active cloud (the fraction of cloud core a_{cc} > 0.01%) gradually increases as shown in Figure 2(a). With the same h, the RH_h corresponding to h is basically the same for the four LES experiments (CON, 1.2ρ_{CON},

https://doi.org/10.5194/acp-2019-273
Preprint. Discussion started: 8 July 2019

$1.4\rho_{CON}$, $1.7\rho_{CON}$). As a result, the differences in the appearance of active cloud among the four experiments can be considered independent of RH_h in this case. Zhu et al (2002) defined local CBL height h_{local} as the height where the gradient of any conserved variable starts to change dramatically. Here the determination of h_{local} is consistent with h, and the penetration depth d_t at any location is defined as the difference between h_{local} and h. Here a_{cp} and a_{ccp} are the projection of the three dimensional cloud and cloud core fields on the XY plane, respectively. Figures 3(a) and (b) show that the proportion of the area of deeper d_t (d_t > 0.3 km) for small ρ is significantly larger than for large ρ (25.67% versus 3.05%). There is a good correspondence between the horizontal distribution of a_{cp} and larger d_t, and for small ρ a cloud core forms only at the location of maximum d_t .

When thermals overshoot into the inversion layer, they become negatively buoyant and decelerate. Compared to the large ρ case, stronger local ascending motion appears (Figure3 (c) X ≈ 5.2 km) for the small ρ case, corresponding to larger overshoot, and greater probability of the air parcel reaching LCL and LFC . Both cloud cover and cloud cores appear in the area of strong ascending motion above the ML. Thus, the areas of cloud fractions a_{cp} and a_{ccp} for small ρ are larger than for large ρ.

4.3 Cloud fraction, vertical velocity and mass flux for varying air density

Three mass flux schemes were used for LES of the Small Cumulus Microphysics Study (SCMS) and Atmospheric Radiation Measurement (ARM) cases: 1. moist static energy convergence closure; 2. Convective available potential energy (CAPE) adjustment; 3. a subcloud convective velocity scaling scheme. The details of the first two schemes are described in Gregory et al (2000). The third scheme was first proposed by Grant (2001) who used turbulent kinetic energy arguments to link the cloud base mass flux to the convective vertical velocity scale of the ML. The three schemes results were compared with the LES results of Negger et al (2004). In general, the third scheme showed a best agreement with LES results in the reproduction of the diurnal variation of the mass flux at cloud base in shallow cumulus convection. However, the algorithm proposed by Grant (2001) produces cloud base mass fluxes too early due to lack of cloud core information. Negger et al (2004) added cloud core fraction to solve this problem. We discuss the effects of air density on cloud or cloud core fraction, vertical velocity and mass flux, and the applicability of the third scheme.

Cuijpers and Bechtold (1995), Neggers et al (2006) and van Stratum (2014) indicated that the cloud fraction at the top of the ML can be estimated by the average

https://doi.org/10.5194/acp-2019-273
Preprint. Discussion started: 8 July 2019

Atmospheric Chemistry and Physics Discussions

saturation deficit $\left(q_{t;h}-\bar{q}_{s;h}\right)$ and the spatial moisture distribution that can be described by specific humidity variance $\sigma_{q;h}$. The $\left(q_{t;h}-\bar{q}_{s;h}\right)$ are the differences between the specific humidity $q_{t;h}$ and the saturation specific humidity $\bar{q}_{s;h}$ at the ML top. The parameterization of the maximum cloud fraction at cloud base a_c is assumed to be:

$$a_c = 0.5 + \alpha \arctan\left(\beta \frac{\left(q_{t;h}-\bar{q}_{s;h}\right)}{\sigma_{q;h}}\right) \tag{7}$$

where the constants α = 0.36, β = 1.55 are used to fit this function to LES results as proposed by Cuijpers and Bechtold (1995). As shown in Figure 4 (a) and (b), for CON and 1.4ρ_{CON}, we see that although the relationship between a_c and $(q_{t;h}-\bar{q}_{s;h})/\sigma_{q;h}$ basically satisfies eq. (7), it also overestimates a_c relative to LES results, especially for smaller a_c (a_c < 5%). The relatively large $\sigma_{q;h}$ for small ρ is an important reason for the high frequency of occurrence of larger a_c, while large $\sigma_{q;h}$ is associated with the entrainment of drier air between the moist thermals. Although a_c generally increases with increasing RH_h, relatively large $\sigma_{q;h}$ is an indispensable condition for the appearance of larger a_c. When $\sigma_{q;h}$ < 0.2 g kg^{-1} and a_c < 5%, a_c is significantly less than that calculated from eq. (7). In the cumulus developmental stage, the thermals with strong ascending motion transport more moisture from the subcloud layer into the cloud layer, thereby significantly increasing a_c. For the single purpose of introducing the first-order feedbacks between core fraction and mass flux, Negger et al (2004) temporarily simplified the relationship between a_c and a_{cc} to linear relation,

$$a_{cc} = \kappa a_c, \tag{8}$$

where κ is a constant (κ = 0.3). In fact, Negger et al (2004) considered κ should be a variable rather than a constant. The factors that can affect the variation of κ should be analyzed and discussed, and on this basis we can build a more sophisticated parameterization of the core fraction.As noted above, Figure 4 (c) and (d) also show a similar trend in that both the areas of a_c and a_{cc} for small ρ are larger than for large ρ. However, with increasing ρ, κ decreases from 0.27 to 0.03.

On the other hand, LeMone and Pennell (1976) observed that cumulus clouds often are deeply rooted in the subcloud layer as dry thermals. Based on the above findings, Neggers et al (2004) proposed a relationship between the convective velocity scale of the subcloud layer w_*, and w_{cc}:

$$w_{cc} \approx \lambda w_* = \lambda \left(\frac{gh}{\Theta_v^0} \overline{\left(w'\theta_v'\right)_s} \right)^{1/3}, \tag{9}$$

https://doi.org/10.5194/acp-2019-273
Preprint. Discussion started: 8 July 2019

where g is the gravitational acceleration, Θ_v^0 is the average virtual temperature of the subcloud layer, and λ is a proportionality factor. Neggers et al (2004) and Ouwersloot et al (2014) proposed that $\lambda \approx 1$, while van Stratum et al (2014) estimated $\lambda \approx 0.84$ based on results from the Dutch Atmospheric LES.

As expected, w_{cc} increases with increasing w_* as shown by the results of three LES experiments (CON, $1.2\rho_{CON}$ and $1.4\rho_{CON}$) in Figure 4(d). However, with increasing ρ, the rate of reduction of w_{cc} is much faster than w_*, and λ decreases from 0.7 to 0.46. The deviation between the results of our sensitivity experiments and previous research increase for increasing ρ. The cases studied by Neggers et al (2004) and van Stratum et al (2013) are at low altitudes, but the results of λ and κ at high altitudes in this study are closer to previous research rather than those at low altitudes. There seems to be a contradiction between the two, and it seems worthwhile to discuss the reason for the large deviation of λ and κ for different values of ρ. The results for $1.7\rho_{CON}$ are not given in Figure 4 due to very small a_{cc}. We found in our sensitivity experiments that the values of λ and κ are determined by the strength of ascending motion within the thermal characterized by w_* and subcloud layer moisture. As shown in Figure 4(e) and (f), when the ascending flow within the thermal reaches the LCL in the drier subcloud layer, there is a relatively small probability of air parcels reaching the LFC due to small latent heat release. In this case the cloud core buoyancy at cloud base height,

$$B_{cc} = \frac{g}{\bar{\theta}_v}\left(\theta_{v,cc} - \bar{\theta}_v\right), \tag{10}$$

B_{cc} is also small (Figure omitted), where $\theta_{v,cc}$ and $\bar{\theta}_v$ are average potential temperature of the cloud core and all grid points at cloud base height, respectively. This results in a more rapid decrease in λ and κ relative to a moister subcloud layer. Larger a_{cc}, w_{cc}, and B_{cc} generate stronger updrafts within the thermals for small ρ, which favors the further development of cumulus as shown in Figure 4(c) and (d). Small ρ to some extent compensates for the drier subcloud layer. In addition, we found that the deviation from multiple sensitivity tests between the values of a_{cc}, w_{cc}, λ and κ for varying ρ increases with decreasing relative humidity in the subcloud layer. The water vapor case for SCMS is moister than that of ARM. Therefore, the reason that Neggers et al (2004) found from LES that $\lambda \approx 1$ for the SCMS case can at least be partly explained.

5 Discussion

Water vapor is relatively abundant over ECMR in summer. However, observations

https://doi.org/10.5194/acp-2019-273
Preprint. Discussion started: 8 July 2019

indicate that high *LCC* occurs mainly over the mid-eastern TP rather than ECMR during summer. Statistical results from ERA-Interim reanalysis data indicate that *LCC* might still be greater than 35% north of 30 °N over the mid-eastern TP for small RH_{2m} (RH_{2m} < 70%), and this is not the case at low altitude. The surface buoyancy flux over the TP is obviously larger than that over lower altitude in eastern China. This density effect is demonstrated with a simple mixed-layer model in Appendix A and further confirmed by LES with the same initial profiles of T, RH and surface layer turbulent fluxes but different values of ρ. That is, reducing ρ increases thermal turbulence and overshooting, which increases the probability of air parcels reaching the LCL and LFC and thus the growth rates of h and RH_h, which favor cloud formation. Stronger ascending motions transport more moisture from the subcloud layer into the cloud layer, and w_{cc} and a_{cc} also increase. The results also indicate that the values of λ and κ are determined by the strength of ascending motion within the thermal that can be characterized by w_* and subcloud layer moisture. Previous research for a drier subcloud layer has suggested that $\kappa = 0.3$ and $\lambda \approx 0.84$, mainly because the smaller latent heat release reduces cloud core formation, which causes a significant decrease in λ and κ. The values of λ and κ for small ρ are significantly larger than for large ρ, especially with a drier subcloud layer. Based on the above analysis, we find that smaller ρ over the TP lead to stronger thermal turbulence which favors the formation and development of convective cloud as demonstrated by the climate statistics of the *LCC* in summer over China as shown in Figure 1. Here we analyzed the effect of only air density on convection and cloud formation. Further studies need to be conducted on the effects of other factors (e.g. vertical wind shear and complicated heterogeneous terrain).

6 Conclusions

The cumulus extent and thermal turbulence over the TP are larger than those over the eastern plain of China. When the relative humidity at 2 m height over the TP is less than 70%, the coverage of low clouds still exceeds 35%, which is rare over the east China plain.

For the same surface sensible heat flux over the TP and the elevated plain, the buoyancy flux over the plateau is larger than over the plain due to the smaller air density which increases the mixing layer height and the relative humidity at the top of the mixed layer. This favors the formation of cumulus clouds over the plateau and increases the probability of the air mass reaching the lifted condensation level and the level of free convection. More water vapor is transported into the clouds from the

https://doi.org/10.5194/acp-2019-273
Preprint. Discussion started: 8 July 2019

subcloud mixed layer, and the rate of cumulus growth is increased.

The values of λ and κ in the subcloud convective velocity scaling mass flux scheme decrease with lower surface relative humidity and weaker thermal turbulence in the subcloud layer, and thus the values obtained from previous studies may not be applicable to a drier subcloud layer or weak thermal turbulence cases.

Appendix A

A SIMPLE MODEL FOR INCORPORATING DENSITY EFFECTS IN THE GROWTH RATE OF THE CONVECTIVE BOUNDARY LAYER

Here we present a simple model to demonstrate that a decrease in surface atmospheric density in the clear convective boundary layer (CBL) increases the growth rate of the CBL depth *h*. The model illustrates how the same surface sensible heat flux $\rho c_p(\overline{wT})_0$ results in an increasing surface buoyancy flux, $(g/T)(\overline{wT})_0$, with decreasing air density ρ. The development utilizes the model of Tennekes (1984) that predicts CBL height *h* and magnitude of the temperature jump ΔT across the CBL top assuming no mean vertical motion in the CBL and horizontal homogeneity. We assume a dry well-mixed CBL so that γ_d - γ = 0, where $\gamma = -dT/dz$ and γ_d = 9.8K km^{-1} is the dry adiabatic lapse rate, throughout the entire CBL and ΔT is assumed to be discontinuous; that is, we assume the entrainment layer has zero thickness. Above *h*, the free troposphere is assumed to have a constant potential temperature lapse rate $\gamma_\theta = \gamma_d - \gamma = d\theta/dz$. This model has been widely used and generally is successful in predicting reasonable values for *h* and ΔT during the rapid growth phase of the daytime CBL at least up to early afternoon and before clouds form with moderate or less mean wind speeds and approximately barotropic conditions.

The model equations start with a relation for the temperature flux at *h*(*t*), $(\overline{wT})_h$, which is equal to the rate at which heat is entrained into the CBL. This yields

$$-(\overline{wT})_h = \Delta T\frac{dh}{dt}. \qquad \text{(A1)}$$

The net rate of change of $\Delta T(t)$ is given by:

$$\frac{d\Delta T}{dt} = \gamma_\theta\frac{dh}{dt} - \frac{\partial\overline{T}}{\partial t}, \qquad \text{(A2)}$$

where $\overline{T}$ is the mean mixed-layer temperature. The rate of change of $\overline{T}$ is given by

$$\frac{\partial\overline{T}}{\partial t} = -\frac{\partial(\overline{wT})}{\partial z} = \frac{(\overline{wT})_0}{h} - \frac{(\overline{wT})_h}{h}, \qquad \text{(A3)}$$

since $(\overline{wT})$ is a linear function of height.

Substitution of (A3) into (A2) yields

https://doi.org/10.5194/acp-2019-273
Preprint. Discussion started: 8 July 2019

$$h\frac{d\Delta T}{dt}=\gamma_\theta h\frac{dh}{dt}-(\overline{wT})_0-\Delta T\frac{dh}{dt}. \quad \text{(A4)}$$

This can be rearranged to

$$\frac{d(h\Delta T)}{dt}=\gamma_\theta h\frac{dh}{dt}-(\overline{wT})_0. \quad \text{(A5)}$$

We integrate (A5) from $t = 0$, which is the start of solar heating in the morning, to the time τ at which we obtain a measurement of h:

$$h\Delta T-h_0\Delta T_0=\frac{1}{2}\gamma_\theta(h^2-h_0^2)-H_\tau/\rho c_p, \quad \text{(A6)}$$

where H_τ is the integrated sensible heat flux,

$$H_\tau=\rho c_p\int_0^\tau(\overline{wT})_0 dt. \quad \text{(A7)}$$

Thus, we have a relationship involving two unknowns: ΔT and h. To reduce this to one unknown, we introduce the relation

$$(\overline{wT})_h=-\beta_1(\overline{wT})_0, \quad \text{(A8)}$$

where the entrainment coefficient β_1 is assumed to be an empirical constant that has been estimated by multiple numerical and observational studies (e.g. Sullivan et al., 1998). Next we modify the first term in (A4) and substitute (A1) and (A8) into this expression to obtain

$$h\frac{d\Delta T}{dt}=h\frac{d\Delta T}{dh}\frac{dh}{dt}=\beta_1 h\frac{d\Delta T}{dh}\frac{(\overline{wT})_0}{\Delta T}. \quad \text{(A9)}$$

We then substitute (A9) into (A4) which yields

$$h\frac{d\Delta T}{dh}+(1+\frac{1}{\beta_1})\Delta T-\gamma_\theta h=0. \quad \text{(A10)}$$

The solution to this is

$$\Delta T h^{\frac{1+\beta_1}{\beta_1}}=\frac{\gamma_\theta}{2+1/\beta_1}h^{(1+\frac{1+\beta_1}{\beta_1})}+C. \quad \text{(A11)}$$

Where C is a constant. In order to give an estimate of the expected magnitude and functional dependencies in (A11), we insert a typical value for β_1 of 0.2 (e.g. Sullivan et al., 1998). Substituting this into (A11), we obtain

$$\Delta T h^6=\frac{\gamma_\theta}{7}h^7+C. \quad \text{(A12)}$$

To evaluate C, we consider that in the morning at $t = 0$, $h(0)$ is very small compared to later in the day, while ΔT changes much less, so that C must also be small compared to $h(\tau)$, especially since h is taken to a very large power, and thus can be neglected as soon as h becomes several times h_0. Therefore,

$$\Delta T\simeq\frac{\gamma_\theta h}{(2+1/\beta_1)}=\frac{\gamma_\theta h}{7}. \quad \text{(A13)}$$

If we again assume h_0 and ΔT_0 are small, from (A6) we have

$$h\Delta T\simeq\frac{1}{2}\gamma_\theta h^2-H_\tau/(\rho c_p). \quad \text{(A14)}$$

Substituting (A13) into (A14),

$$h^2 \simeq 2H_\tau \frac{(2\beta_1+1)}{\gamma_\theta \rho c_p}. \tag{A15}$$

This gives us a relation to estimate the CBL height at a specific location given the integrated temperature flux from the initiation of surface heating in the morning to a time τ presumed to be before mid-afternoon when the surface heating has dropped significantly from its mid-day maximum. Alternatively, it may also be possible to use (A15) to estimate H_τ if h and γ_θ are known.

We now apply (A15) to estimate the effect of air density ρ on h. Here we assume two CBL heights: one at sea level h_0 and the other at h. We further assume that the integrated sensible heat flux at each location is the same, that is, $H_\tau = H_{\tau 0}$. From the hydrostatic equation, we have

$$\frac{dp}{p} = -\frac{g}{R_d T} dz = -\frac{g}{R_d (T_0+\gamma z)} dz, \tag{A16}$$

where z is the surface elevation above sea level, R_d = 287.06 J kg^{-1} K^{-1} is the dry air gas constant, and g = 9.807 m s^{-2} is the gravitational acceleration. From the ideal gas law,

$$\frac{d\rho}{\rho} = \frac{dp}{p} - \frac{dT}{T}. \tag{A17}$$

Then, substituting (A16) into (A17) we obtain

$$\frac{d\rho}{\rho} = -\frac{g}{R_d} \frac{dz}{(T_0+\gamma z)} - \gamma \frac{dz}{(T_0+\gamma z)} = -\left(\frac{g}{\gamma R_d}+1\right) \frac{\gamma dz}{(T_0+\gamma z)}. \tag{A18}$$

Integrating from z = 0 to z,

$$\frac{\rho}{\rho_0} = \left(\frac{T_0+\gamma z}{T_0}\right)^m, \tag{A19}$$

where $m = -\left(\frac{g}{\gamma R_d}+1\right)$.

Substituting h at height z and h_0 at height z_0 = 0 into (A15) and taking the ratio of the heights, we have

$$h/h_0 = (\rho/\rho_0)^{-1/2} = \left(\frac{T_0+\gamma z}{T_0}\right)^{-m/2}, \tag{A20}$$

As a demonstration of the impact of γ on h/h_0 we show in Figure A1 how h/h_0 changes with z for different values of γ_θ starting with the lowest level in Table B1 of Appendix B and decreasing to a value close to that of the second level, *i.e.*: γ_θ= {20, 14, 8, 2}K km^{-1} or γ = {-10.2, -4.2, 1.8, 7.8} K km^{-1}. Here we assume that the entire layer through which we calculate h has the same γ_θ, and standard atmosphere values of T_0 = 288.16K and ρ_0 = 1.225 kg m^{-3}. We see a strong dependency of h/h_0 on γ_θ; for example, h/h_0 is almost 20% larger than its sea level value at 4 km elevation for γ_θ = 20 K km^{-1} and more than 30% larger for γ_θ = 2 K km^{-1}.

https://doi.org/10.5194/acp-2019-273
Preprint. Discussion started: 8 July 2019

Atmospheric Chemistry and Physics Discussions

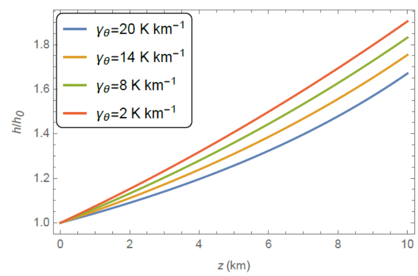

Figure A1. Ratio of the CBL height at an elevation z versus height at sea level for $\gamma = 20$ (blue), = 14 (orange), = 8 (green), 2 (red) K km^{-1}.

Appendix B

THE LES MODEL DESCRIPTION AND SIMULATION SETUP, AND A COMPARISON BETWEEN THE OBSERVATIONS AND THE LES

The LES experiments discussed here were performed with the Dutch Atmospheric LES (DALES) (Heus et al. 2010) using the Deardorff subgrid-scale closure (Deardorff, 1973) and a second-order advection scheme for scalars, momentum, and turbulence kinetic energy. We used the radiation scheme proposed by Fu and Liou (1993) and Pincus and Stevens (2009), and a simple ice microphysics scheme (Grabowski, 1998) that considers the impact of the relatively low temperatures over the TP on ice phase microphysical processes. A resolution of 6.4 km x 6.4 km x 6.0 km with 256 x 256 x 150 grid points is used, with a total integration time of 50400 s. Zhang et al (2017) pointed out that an effective way to simulate shallow cumulus is by building a composite modeling case (average values of multiple "golden days"). Using this method, we attempted to construct the initial profiles, surface turbulent fluxes and large-scale forcing in the control experiment (CON) by selecting nine shallow cumulus days at Nagqu over TP. In order to reduce the differences between the LES and the observations, 9-day means were slightly modified. We adopted the method proposed by van der Dussen et al (2013) to construct the initial profiles of virtual potential temperature θ_v and specific humidity q_T by dividing them into 3 linear segments,

$$\varphi(z) = \begin{cases} \varphi_1 + z\Gamma_{\varphi_1} & 0\ \mathrm{km} < z \le 0.5\ \mathrm{km} \\ \varphi_1 + 0.5\Gamma_{\varphi_1} + (z-0.5)\Gamma_{\varphi_2} & 0.5\ \mathrm{km} < z \le 4\ \mathrm{km}, \\ \varphi_1 + 0.5\Gamma_{\varphi_1} + (4-0.5)\Gamma_{\varphi_2} + (z-4)\Gamma_{\varphi_3} & 4\ \mathrm{km} < z \le 6\ \mathrm{km} \end{cases} \quad \text{(B1)}$$

with the constants given in Table B1. Where $\varphi \in \{q_T, \theta_v\}$ are the total specific humidity and the virtual potential temperature, respectively.

https://doi.org/10.5194/acp-2019-273
Preprint. Discussion started: 8 July 2019

Table B1 Values of the constants which are used to describe the initial profiles shown in Figure S1

$\Gamma_{q_{T1}}\left(\mathrm{g\ kg^{-1}\ km^{-1}}\right)$	$\Gamma_{q_{T2}}\left(\mathrm{g\ kg^{-1}\ km^{-1}}\right)$	$\Gamma_{q_{T3}}\left(\mathrm{g\ kg^{-1}\ km^{-1}}\right)$	$q_{T1}\left(\mathrm{g\ kg^{-1}}\right)$
-2.4	-0.89	-0.2	4.8
$\Gamma_{\theta_{v1}}\left({}^{\circ}\mathrm{K\ km^{-1}}\right)$	$\Gamma_{\theta_{v2}}\left({}^{\circ}\mathrm{K\ km^{-1}}\right)$	$\Gamma_{\theta_{v3}}\left({}^{\circ}\mathrm{K\ km^{-1}}\right)$	$\theta_{v1}\left({}^{\circ}\mathrm{K}\right)$
20	2.29	5.5	320

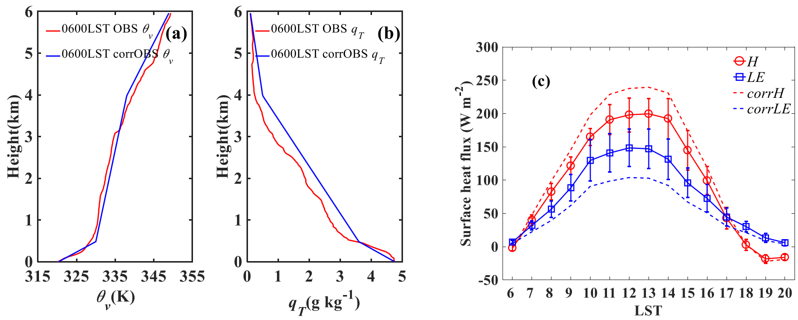

Figure B1 Vertical profiles of (a) θ_v and (b) q_T at 06:00 LST. The red and blue lines are the observations and LES initial profiles, respectively. (c) The solid red and blue lines are the nine-day averaged sensible heat flux *H* and latent flux *LE*, respectively, calculated by the eddy covariance method. Error bars represent standard deviations. The dashed red and blue lines are the “corrected” sensible heat fluxes *corrH* and latent fluxes *corrLE*.

As shown in Figure B1, the diurnal maximum of both the sensible heat flux *H* and the latent flux *LE* at Nagqu occur at roughly the same time (12:00 LST), and *H* is larger than *LE* during the daytime. However, compared to the radiosonde observations at 12:00 LST and 18:00 LST, we find poor agreement between the LES results and the observations when we directly use the *H* and *LE* data calculated by the eddy covariance method without any corrections. The comparison results show that within the boundary layer q_T is overestimated by 2 g kg^{-1} while θ_v is underestimated by 4 °K. To adddress this, we increased *H* by 20%, and decreased *LE* by 25%; we call these corrected values *corrH* and *corrLE*.

Figures B2(a) and (b) show that the geostrophic wind direction changes counterclockwise from southeast in the surface layer to northwest in upper levels in response to the cold advection. As shown in Figures B2(d) and (e), from 06:00 LST to 16:00 LST, the cooling rate caused by weak cold air advection at all levels generally did not exceed 1 °K day^{-1}, and dry advection below 450 hPa was about 0.5 g kg^{-1} day^{-1}; thus, temperature and moisture advection were negligible. As shown in Figure

https://doi.org/10.5194/acp-2019-273
Preprint. Discussion started: 8 July 2019

B2(c), the vertical temperature and moisture transport due to large scale subsidence can result in about 1-2 °K warming and 0.5 g kg^{-1} drying after 10 hours.

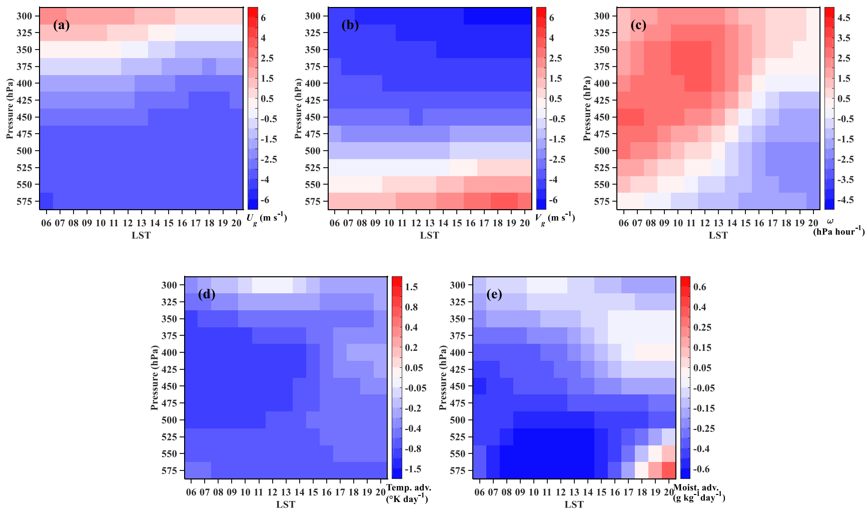

Figure B2 Time–height composite-mean large-scale for geostrophic wind components (a) U_g, (b) V_g, (c) subsidence rate ω, (d) temperature advection, and (e) moist advection for the composite case based on nine days continuous forcing data from ERA-Interim reanalysis data.

We carried out an LES control experiment (CON) and two sets of sensitivity experiments: The first set, 1.2ρ_{CON}, 1.4ρ_{CON}, and 1.7$\rho_{CON,}$ have air densities ρ altered by the factor r_1 compared to CON but with the same profiles of θ_v and relative humidity. The second set, 1.4$\rho_{CON}RH$0.05, 1.4$\rho_{CON}RH$0.15, and 1.4$\rho_{CON}RH$0.3, have different relative humidities below 1.5 km, increasing from RH_{CON} to RH_{CON} + (1 - RH_{CON}) x r_2 for the 1.4ρ_{CON} case. RH_{CON} is the relative humidity for control experiment (CON), and the values of r_1 and r_2 are shown in Table B2.

Table B2 Specifications for the LES sensitivity experiments

	r_1	r_2
CON	1.0	0.0
1.2ρ_{CON}	1.2	0.0
1.4ρ_{CON}	1.4	0.0
1.7ρ_{CON}	1.7	0.0
1.4$\rho_{CON}RH$0.05	1.4	0.05
1.4$\rho_{CON}RH$0.15	1.4	0.15
1.4$\rho_{CON}RH$0.3	1.4	0.3

Figure B3 shows that the LES model can reproduce the general tendencies and the

https://doi.org/10.5194/acp-2019-273
Preprint. Discussion started: 8 July 2019

Atmospheric Chemistry and Physics
Open Access
Discussions

diurnal variation of θ_v and q_T at Nagqu, which indicates that the large-scale forcing has been correctly specified. There are minor differences between the observations and the LES; the absolute value of q_T differences generally do not exceed 0.5 g kg^{-1}, and the LES underestimates θ_v by 1-3 K.

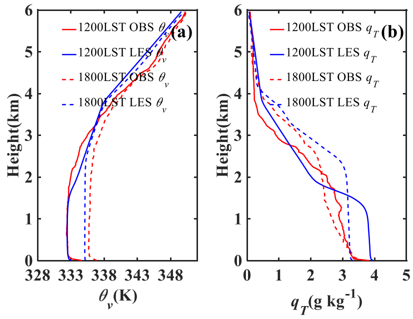

Figure B3 Vertical profiles of (a) θ_v and (b) q_T at 12:00 LST (solid line) and 18:00 LST (dash line) at the Nagqu site. The red and blue lines represent the observed profiles from radiosondes and the simulated profiles from CON, respectively.

Data availability. The reanalysis data were from ECMWF (European Centre for Medium-Range Weather Forecasts), which is available at https://apps.ecmwf.int/datasets/data/interim-full-mnth/levtype=sfc/ and https://apps.ecmwf.int/datasets/data/interim-full-daily/levtype=sfc/. The original codes of DALES (Dutch Atmospheric Large Eddy Simulation) were publicly available at https://github.com/dalesteam/dales. All the original datasets and code needed to reproduce the simulation results shown in this paper are available upon request via email: wyj@cma.gov.cn.

Author contributions. YW was responsible for collecting and processing the data, and manuscript and plot preparation. YW, XX and MZ designed the experiments. YW, XX, MZ, and DL analyzed the data. YW wrote the paper. DL wrote Appendix A. All authors contributed to measurements, discussed results, and commented on the paper.

Competing interests. The authors declare that they have no conflict of interest.

Acknowledgements. This study is supported by the Second Comprehensive and Scientific Investigation and Study of Tibetan Plateau. This study is also supported by National Natural Science Foundation of China (Grant Nos. 91837310), the National Natural Science Foundation for Young Scientists of China (Grant Nos. 41805006), Basic Research Special Project of Chinese Academy of Meteorological Sciences (2018Y008), and National Natural Science Foundation of China (Grant Nos. 91637102). The National Center for Atmospheric Research is sponsored by the U. S. National Science Foundation.

https://doi.org/10.5194/acp-2019-273
Preprint. Discussion started: 8 July 2019

Atmospheric Chemistry and Physics Discussions

References

Betts, A. K.: Non-precipitating cumulus convection and its parameterization. Quart. J. Roy. Meteor. Soc., 99, 178-196, https://doi.org/10.1002/qj.49709941915, 1973.

Cuijpers, J. W. M., and Bechtold., P.: A simple parameterization of cloud water related variables for use in boundary layer models. J. Atmos. Sci. *52*, 2486-2490, https://doi.org/10.1175/1520-0469(1995)052<2486:ASPOCW>2.0.CO;2, 1995.

Dai, J. X.: Climate of the Tibetan Plateau (in Chinese). Beijing: China Meteorological Press. 365, 1990.

Deardorff, J. W.: Three-dimensional numerical modeling of the planetary boundary layer, in: Workshop on Meteorology, edited by: Haugen, D. A., American Meteorological Society, 271-311, 1973.

Fu, Q., and Liou, K. N.: Parameterization of the radiative properties of cirrus clouds, J. Atmos. Sci., 50(13), 2008-2025, https://doi.org/10.1175/1520-0469(1993)050<2008:POTRPO>2.0.CO;2, 1993.

Heus, T., van Heerwaarden, C. C., Jonker, H. J. J., Pier Siebesma, A., Axelsen, S., van den Dries, K., Geoffroy, O., Moene, A. F., Pino, D., de Roode, S. R., and Vilà-Guerau de Arellano, J.: Formulation of the Dutch Atmospheric Large-Eddy Simulation (DALES) and overview of its applications, Geosci. Model Dev., 3, 415-444, https://doi.org/10.5194/gmd-3-415-2010, 2010.

Grabowski, W. W.: Toward Cloud Resolving Modeling of Large-Scale Tropical Circulations: A Simple Cloud Microphysics Parameterization, J. Atmos. Sci., 55(55), 3283-3298, https://doi.org/10.1175/1520-0469(1998)055<3283:TCRMOL>2.0.CO;2, 1998.

LeMone, M. A., and Pennell, W. T.: The relationship of trade wind cumulus distribution to subcloud layer fluxes and structure. Monthly Weather Review, 104(5), 524-539, https://doi.org/10.1175/1520-0493(1976)104<0524:TROTWC>2.0.CO;2, 1976.

Li, Y. Y., and Zhang, M. H.: Cumulus over the Tibetan Plateau in the summer based on CloudSat–CALIPSO data. J. Climate, 29, 1219-1230, https://doi.org/10.1175/JCLI-D-15-0492.1, 2016.Neggers, R. A. J., Siebesma, A. P., Lenderink, G., and Holtslag, A.A.M.: An evaluation of mass flux closures for diurnal cycles of shallow cumulus. Mon. Wea. Rev. 132, 2525-2538, https://doi.org/10.1175/MWR2776.1, 2004.

Neggers, R., Stevens, B., and Neelin, J. D.: A simple equilibrium model for shallow-cumulus-topped mixed layers. Theoretical and Computational Fluid

https://doi.org/10.5194/acp-2019-273
Preprint. Discussion started: 8 July 2019

Atmospheric Chemistry and Physics
Open Access
Discussions

Dynamics, 20(5-6), 305-322, https://doi.org/10.1007/s00162-006-0030-1, 2006.

Ouwersloot, H. G., Vilà-Guerau de Arellano, J., Nölscher, A. C., Krol, M. C., Ganzeveld, L. N., Breitenberger, C., Mammarella, I., Williams, J., and Lelieveld, J.: Characterization of a boreal convective boundary layer and its impact on atmospheric chemistry during HUMPPACOPEC-2010, Atmos. Chem. Phys., 12, 9335-9353, doi:10.5194/acp-12-9335-2012, 2012.

Grant, A. L. M.: Cloud-base fluxes in the cumulus-capped boundary layer. Quart. J. Roy. Meteor. Soc., 127, 407–422, doi: 10.1002/qj.49712757209, 2001.

Gregory, D., J.-J. Morcrette, C. Jakob, A. C. M. Beljaars, and T. Stockdale: Revision of convection, radiation and cloudschemes in the ECMWF Integrated Forecasting System. Quart. J. Roy. Meteor. Soc., 126, 1685–1710, doi:10.1002/qj.49712656607, 2000.

Pincus, R., and Stevens., B.: Monte Carlo spectral integration: A consistent approximation for radiative transfer in large eddy simulations, J. Adv. Model. Earth Syst., 1, https://doi.org/10.3894/JAMES.2009.1.1, 2009.

Stull, R. B.: An Introduction to Boundary Layer Meteorology. Dordrecht : Kluwer Academic Publishers. 666, 1988.

Sullivan, P. P., Moeng, C. H., Stevens, B., Lenschow, D. H., and Mayor, S. D.: Structure of the entrainment zone capping the convective atmospheric boundary layer. Journal of Atmospheric Sciences, 55(19), 3042-3064, https://doi.org/10.1175/1520-0469(1998)055<3042:SOTEZC>2.0.CO;2, 1998.

Sugimoto, S. and Ueno, K.: Role of mesoscale convective systems developed around the Eastern Tibetan Plateau in the eastward expansion of an upper tropospheric high during the monsoon season, J. Meteol. Soc. Japan, 90, 297-310, doi:10.2151/jmsj.2012-209, 2012.

Tennekes, H.: A Model for the Dynamics of the Inversion Above a Convective Boundary Layer. J. Atmos. Sci., 30, 558-567, https://doi.org/10.1175/1520-0469(1973)030<0558:AMFTDO>2.0.CO;2, 1984.

van der Dussen, J. J., de Roode, S. R., Ackerman, A. S., Blossey, P. N., Bretherton, C. S., Kurowski, M. J., Lock, A. P., Neggers, R. A. J., Sandu, I., and Siebesma., A. P.: The GASS/EUCLIPSE model intercomparison of the stratocumulus transition as observed during ASTEX: LES results, J. Adv. Model. Earth Syst., 5, 483-499, 2013, doi:10.1002/jame.20033.

Van Stratum, B. J. H., Vilá-Guerau de Arellano, Jordi, Van Heerwaarden, C. C., and Ouwersloot, H. G.: Subcloud-layer feedbacks driven by the mass flux of shallow cumulus convection over land. J. Atmos. Sci., 71, 881-895,

https://doi.org/10.5194/acp-2019-273
Preprint. Discussion started: 8 July 2019

https://doi.org/10.1175/JAS-D-13-0192.1, 2014.

Wang, Y. J., Xu, X. D., Liu, H. Z., Li, Y. Q., Li, Y. H., Ze, Z. Y., Gao, X. Q., Ma, Y. M., Sun, J. H., Lenschow, D. H., Zhong, S. Y., Zhou, M. Y., Bian, X. D., and Zhao. P.: Analysis of land surface parameters and turbulence characteristics over the Tibetan Plateau and surrounding region, J. Geophys. Res. Atmos., 121, 9540-9560, doi: 10.1002/2016JD025401, 2016.Xu, X. D., Zhou, M. Y., Chen, J. Y., Bian, L. G., Zhang, G. Z., Liu, H. Z., Li, S. M., Zhang, H. H., Zhao, Y. J., Suolongduoji, Wang, J. Z.: A comprehensive physical pattern of land-air dynamic and thermal structure on the Qinghai-Xizang Plateau. Sci. China, Ser. D, 45(7): 577-594, doi: 10.1360/02yd9060, 2002.

Xu, X. D., Zhang, R. H., Koike, T., Lu, C. G., Shi, X. H., Zhang, S. J., Bian, L. G., Cheng, X. H., Li, P. Y., and Ding, G. A.: A new integrated observational system over the Tibetan Plateau. Bull. Amer. Meteor. Soc., 89(10), 1492-1496, doi: 10.1175/2008BAMS2557.1, 2008.

Xu, X. D., Shi, X. H. and Lu, C. G.: Theory and Application for Warning and Prediction of Disastrous Weather Downstream from the Tibetan Plateau, Novinka Science Publishers, Inc. New York, 2012.

Zhang, Y., Klein, S. A., Fan, J., Chandra, A. S., Kollias, P., Xie, S., and Tang, S. Q.: Large-Eddy Simulation of Shallow Cumulus over Land: A Composite Case Based on ARM Long-Term Observations at Its Southern Great Plains Site, J. Atmos. Sci., 74, 3229-3251, https://doi.org/10.1175/JAS-D-16-0317.1, 2017.

Zhou, M. Y., Xu, X. D., Bian, L. G., Chen, J, Y., Liu, H. Z., Zhang, H. S., Li, S. M., and Zhao, Y. J.: Observational analysis and dynamic study of atmospheric boundary layer on Tibetan Plateau (in Chinese). Beijing: China Meteorological Press. 125, 2000.

Zhu, P., and Albrecht., B. A.: A theoretical and observational analysis on the formation of fair-weather cumuli. J. Atmos. Sci., 59, 1983-2005, https://doi.org/10.1175/1520-0469(2002)059<1983:ATAOAO>2.0.CO;2, 2002.

Figure

https://doi.org/10.5194/acp-2019-273
Preprint. Discussion started: 8 July 2019

Atmospheric Chemistry and Physics
Discussions

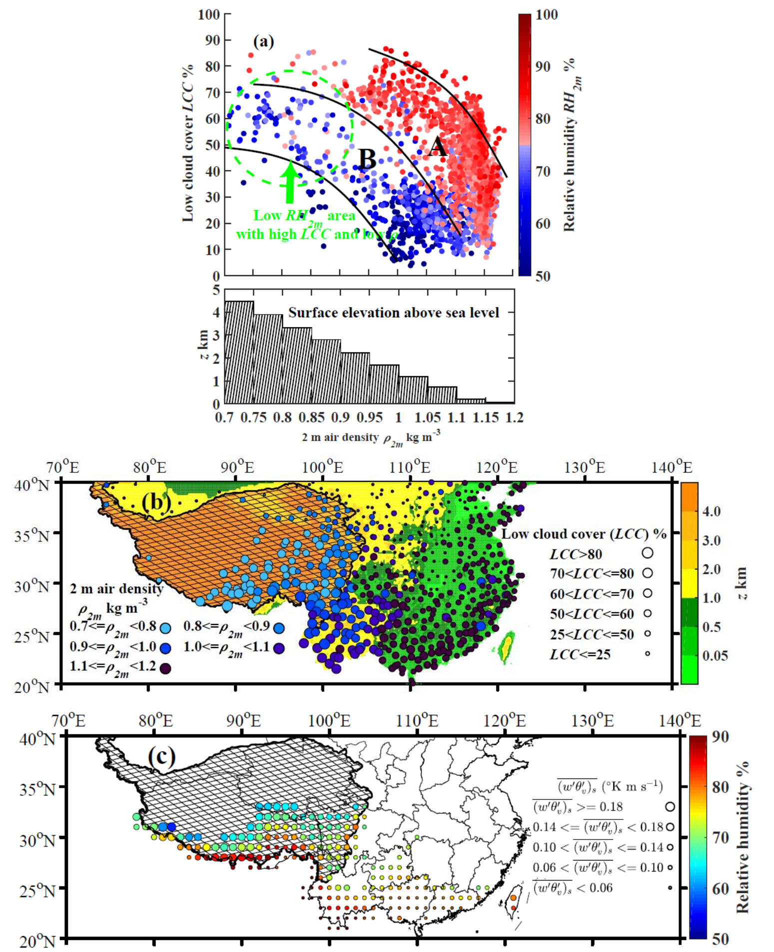

Fig. 1 (a) The relationships among monthly means of *LCC*, ρ_{2m} and RH_{2m} observed by the AWS in summer. The samples are divided into two groups: RH_{2m} > 75% (red dots) and RH_{2m} < 75% (blue dots). A region and B region generally correspond to RH_{2m} both greater than and less than 75%, respectively. The histogram shows an approximate relationship between ρ_{2m} and surface elevation above sea level *z* at the bottom of Figure 1 (a). (b) The spatial distribution of the observed monthly mean *LCC*. (c) The spatial distribution of monthly means of relative humidity and surface virtual potential temperature flux in the surface layer with *LCC* greater than 35% from ERA-interim data from 9:00 LST to 15:00 LST (3:00 UTC to 9:00 UTC). The TP is the cross-hatched area (altitude > 2500 m) in Figures 1(b) and (c).

https://doi.org/10.5194/acp-2019-273
Preprint. Discussion started: 8 July 2019

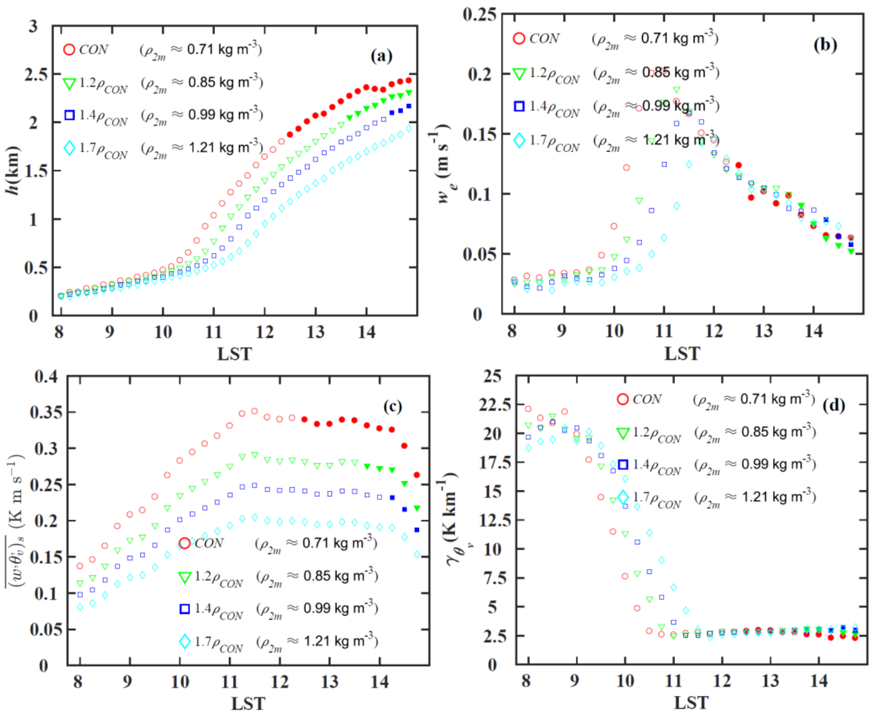

Fig. 2 The time variations of (a) h, (b) w_e, (c) surface virtual potential temperature flux, and (d) γ_{θ_v} for four LES experiments (CON, 1.2ρ_{CON}, 1.4ρ_{CON} , 1.7ρ_{CON}) before the early stage of cloud core formation. Solid and hollow symbols represent the presence or absence of cloud core, respectively.

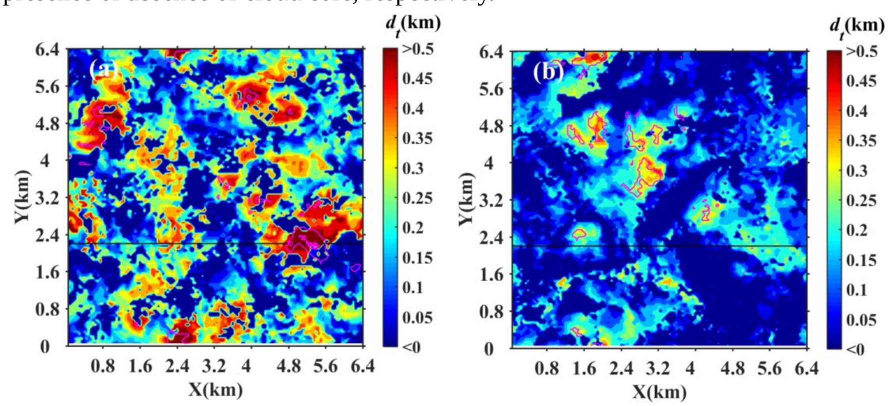

https://doi.org/10.5194/acp-2019-273
Preprint. Discussion started: 8 July 2019

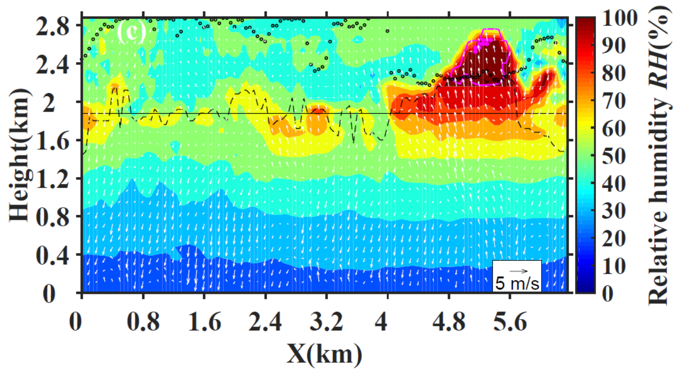

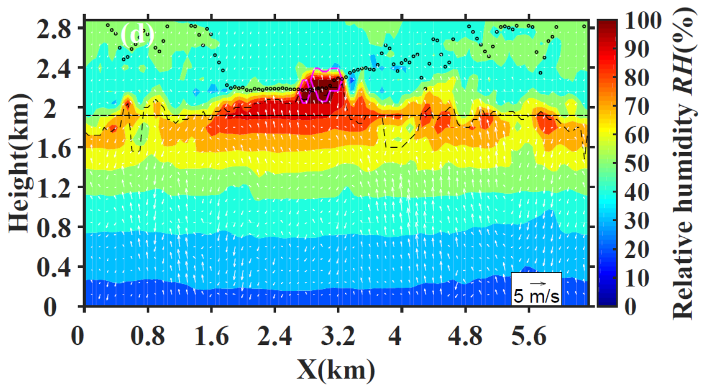

Fig. 3 The horizontal distribution of d_t (color shaded) for $h \approx 1.85$ km for two LES experiments (a) CON at 12:52 LST (b) $1.4\rho_{CON}$ at 14:10 LST. The area enclosed by the pink line and solid circles delineate a_{cp} and a_{ccp}. The solid straight lines in Figures (a) and (b) represent the projection of the XZ plane in Figures (c) and (d) on the XY plane, respectively. The vertical cross-section (XZ-plane) of relative humidity (color shaded) and wind vectors (X-axis wind speeds are ten times smaller than true values) for two LES experiments: (c) CON (d) $1.4\rho_{CON}$ obtained along the black solid lines in Figure 3(a) and (b), respectively. Hollow circles represent the lifting condensation level of the grids in the X-direction at the height of the mixed layer $z_{lcl}(h)$, and the pink line and solid circles have the same meaning as in Figure 3 (a) and (b).

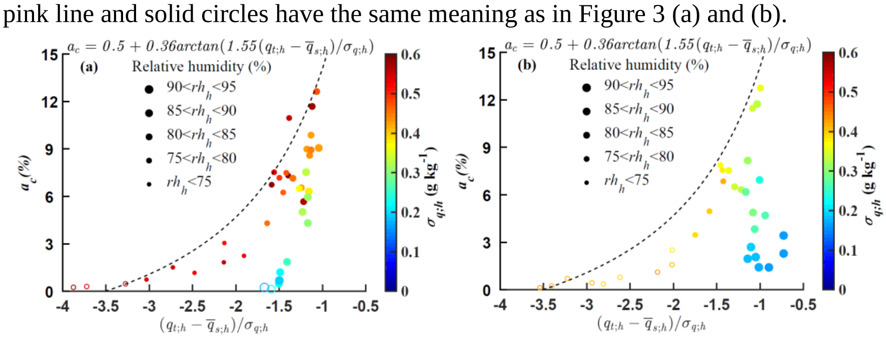

https://doi.org/10.5194/acp-2019-273
Preprint. Discussion started: 8 July 2019

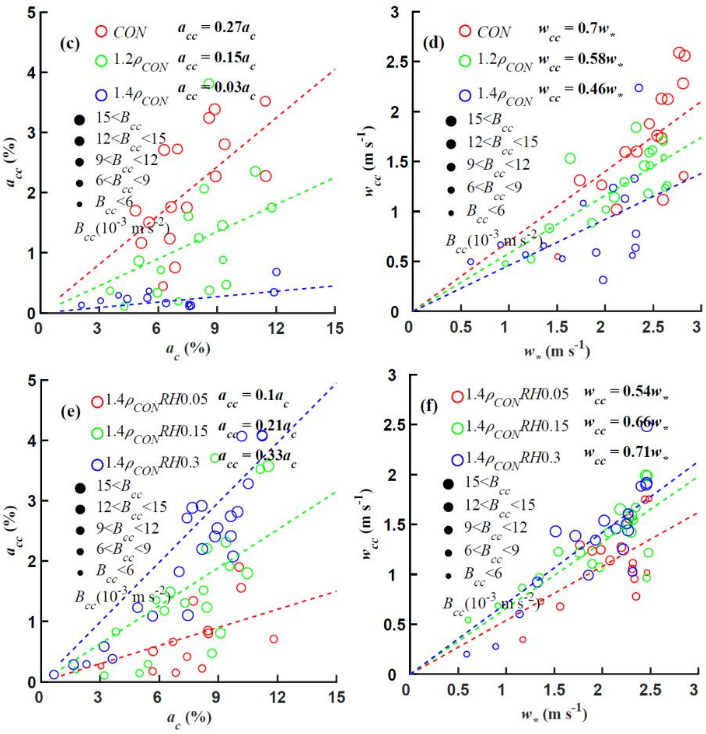

Fig. 4 Scatter diagrams of a_c versus $(q_{t;h} - \overline{q}_{s;h})/\sigma_{q;h}$ for two LES experiments (a) CON (b) 1.4ρ_{CON}. The black dashed lines are from eq. (7), and the color and the size of the points represent the values of $\sigma_{q;h}$ and RH_h, respectively. Scatter diagrams of (c) a_c versus a_{cc} and (d) w_* versus w_{cc} are shown for three LES experiments (CON, 1.2ρ_{CON}, 1.4ρ_{CON}). The color identifies the experiments and the size of the points represents the cloud core buoyancy at cloud base B_{cc}. Figure 4 (e) and (f) are the same as Figure 4 (c) and (d), respectively, but for the three LES experiments (1.4$\rho_{CON}$$RH$0.05, 1.4$\rho_{CON}$$RH$0.15, 1.4$\rho_{CON}$$RH$0.3)